Multi-pulse decomposition for nonlinear seismic analysis of structural systems

Ehsan Ahmadi*[1], Mohammad R. Salami[1], Raffaele De Risi[2], Mohammad M. Kashani[3], Nicholas A. Alexander[2]
1. Faculty of Engineering and the Built Environment, Birmingham City University, UK
2. Department of Civil Engineering, University of Bristol, UK
3. Faculty of Engineering and Physical Sciences, University of Southampton, UK
* Corresponding Author, email: ehsan.ahmadi@bcu.ac.uk

Abstract

Large sympathetic, resonance-like, structural behaviour to earthquake excitations with analogous frequency content often plays a critical role in determining its maximum seismic response. Earthquake excitation typically contains a broad spectrum of non-stationary frequency content, wave packets, which are difficult to observe from the recorded time series. Therefore, identifying the root cause of large responses (which act sympathically with the input but do not achieve full-resonance) of a structure is problematic. Hence, this paper proposes a new multi-pulse decomposition method of ground motions, through which components of a ground motion within a specific period range are determined. In this method, a ground motion is approximated with a Gauss-Fourier wave packet series. The decomposed components, wave packets, contain information about it's time-position, frequency, amplitude, pulse width and phase angle. Unlike the Ricker (Morlet) wavelet the Gauss-Fourier wave packet is not limited to symmetrical pulses. One ensemble of 40 near-fault ground motions and one ensemble of 44 far-fault ground motions are used to demonstrate the application and efficiency of the proposed method. The method is shown to be precise in reconstructing the original ground motion using its decomposed components. It is also concluded that the method is accurate in replication of elastic and inelastic response spectra of ground motions within a specific period range. It is demonstrated that for some structure/ground motion combinations, only a few Gauss-Fourier components are required to faithfully describe response behaviour. This highlights that, for these systems, most of the recorded earthquake time series acts like noise on a much simpler wave-packet signal.

Keywords: Ground motion decomposition; ground motion reconstruction; Gaussian-Fourier series; multi-pulse; Gabor wavelet; dominant components; elastic and inelastic response spectra regeneration; Genetic Algorithm

1. Introduction

1.1 Background

In the earthquake-resistant design of structures, critical excitation methods are very prominent ([1], [2],[3]). For a linear elastic structure, the coincidence of natural modal frequencies with the frequencies of the dominant components of a ground motion can lead to a critical seismic response of a structure consisting of a sympathetic resonance-like behaviour. The term 'sympathetic' denotes an effect which arises in the response that is caused by a particular feature of the input. This response is only 'resonance-like' because not enough cycles of forcing are present to achieve full resonance. Typical Fourier spectral analysis can determine the magnitude, averaged in time, of these dominant frequency components in the ground motion, and standard eigenvalue analysis can determine the modal frequencies of the structure. Note that the time-localized nature of these dominant frequency components (which are non-stationary) cannot be estimated using standard Fourier spectral methods. Nevertheless, for a linear structural system, an application of a Fourier transform to the equations of motion effectively converts it from a set of linear differential equations to a set of linear algebraic equations; thus, the analysis, for this case, is considered accurate. Therefore, the loss of information (i.e. the pulse arrival time, intensity, and duration) does not affect the accuracy of calculating the

structural responses. In addition, the modal participation factors tend to reduce in magnitude with increasing mode number strongly suggesting only a few modes need to be considered.

As ground motion amplitudes increase, structures are pushed, by design, from linear to nonlinear (plastic) response behaviour. A Fourier transform of the equations of motion no longer yields a set of linear algebraic equations. Thus, inferences (such as modal superposition for linear systems) is no longer necessarily valid for nonlinear systems. During the plastic, ductile, deformation phase, two types of localization can be observed. Firstly, spatial localization of plastic hinges typically occurs in the beams of the bottom storeys of a well-designed building. This localization, it has been suggested, tends to mathematically project the dynamic responses onto a much lower dimensional sub-space involving only one or two 'modes' ([4], [5]). Note also that orthogonality and superposition of 'modes' for a nonlinear system are no longer mathematically correct. The second type of localization is in time. The phases of ductile deformation occur at specific times generating an increase in energy losses. This also causes a reduction in stiffness and hence a time-localised large reduction in the averaged 'modal' periods. The interaction between instantaneous period and damage can be quite complex ([6],[7]).

Therefore, since spatiotemporal localization is important for a nonlinear structural system, this research aims to generate a new decomposition of the earthquake time series that involves the sum of time-localized wave-packets rather than time-invariant (averaged) Fourier components. As the spatial structural localization cause by ductility tends to limit the number of 'modes' that influence the nonlinear responses, we seek a new decomposition that is also frequency band-limited to a range likely to affect only these 'modes'. Thus, this decomposition will seek to identify pulses within the ground motion time series, their magnitude/duration and when they arrive for a given nonlinear structural system. Note that the decomposition while being performed on the ground motion alone must implicitly assume a particular structural application context.

1.2 Existing decomposition methods

Strong ground motions, particularly near-fault ground motions, can have very detrimental effects on structures ([8],[9]). Some researchers used simple waveforms to extract the dominant components of a ground motion. These waveforms include piece-wise triangular functions ([10],[11]), sinusoidal functions [12], and multi-parameter decaying functions [13]. With the emergence of advanced signal analysis approaches, more novel methods were developed to identify the dominant component of a ground motion. Vassiliou and Makris (2011), in their seminal work, employed an analysis based on the continuous wavelet transform to identify the most correlated time-frequency position for a Ricker wavelet [14]. However, this approach has limitations, which stem from the wavelet transform (cross-correlation function) and the symmetrical mother wavelet employed, and will be more fully discussed in section 2.1. In addition, they only extracted single pulses and did not develop a robust algorithm for multi-pulse extraction. Baker (2007) extracted the dominant velocity component of a ground motion using wavelet analysis [15]. The Daubechies wavelet of order 4 was selected as the mother wavelet since it approximates the shape of many dominant velocity pulses. However, the wavelet analysis is highly dependent on the type of mother wavelet chosen, and the results of the ground motion decomposition can be very different using various mother wavelets [16]. Given the shortcoming of the wavelet analysis, some researchers used the empirical decomposition method (EMD) to decompose a ground motion ([17],[18]). The ground motion is split into high-frequency and low-frequency components, and the dominant component is determined by fitting a simple waveform to the low-frequency component ([19],[20],[21],[22]). Some others adopted principal component analysis and genetic algorithm to improve the efficiency of the ground motion decomposition ([23],[24]).

All these existing decomposition methods are for the identification of a single dominant component. However, a ground motion might include multiple dominant components, which need to be considered to achieve a more accurate approximation of the ground motion. Additionally, these single dominant components are extracted regardless of the 'modal' periods of the structure, and so, critical resonant-like amplified responses might not be achieved in a structure. For instance, in Baker's method [15], the residual component of the ground motion (the pulse component subtracted from the original ground

motion) was found to affect the response of structures significantly. In some cases, for ground motions with pulses far from the natural periods of the structure, the residual component resulted in larger structural responses than the pulse ([25],[26]).

Thus, given that a single pulse is unlikely to be accurate for an arbitrary structural system, the questions are two-fold (i) how a multi-pulse, time-localized decomposition of an earthquake can be obtained and (ii) how many components are really necessary for an effective analysis of nonlinear structural systems?

1.3 Research Contribution

As the above literature survey demonstrated, the identification of a dominant component of ground motions (i.e. pulse-like/non-pulse-like) has received much attention. Nevertheless, there is a need to develop a more general method for a time-localized, frequency bandwidth limited, multi-component decomposition of ground motions. As sympathetic, resonance-like behaviour may be a key issue in seismic response estimation of structures, the frequency content of the structure needs to be considered in the identification of dominant pulse components of a ground motion.

The numerical algorithms behind both the discrete Fourier and Wavelet transforms are designed for maximal computational efficiency. Both algorithms make full use of the Cooley-Tukey Fast Fourier Transform algorithm [27]. The wavelet transform is a cross-correlation function between signal and mother wavelet. It conventionally operates as a complex function of only two parameters namely time-scale and time-shift of the mother wavelet. This is attractive as ploting a 2-D contour plot could enable the identification of the optimal position/scale of the mother wavelet relative to the signal (as in [14]). However, if we want to make further adjustments to the shape of the mother wavelet, by not assuming a particular symmetry, non-frequency dependant wavelet width, amplitude-scaling and skew, this would require additional parameters to be explored. Therefore, using the wavelet transform to obtain the optimal set of parameters for this higher dimensional space is not so efficient.

In this study, a minimal parametric representation of a ground motion is sought that: (*i*) is based on a set of parametrically defined functions, and (*ii*) is a transformation of a ground motion onto some subspace with a dimension far smaller than the ground motion itself. This expansion of a ground motion comprises a limited number of components that are localized in time and have a consistent functional form. Thus, in this approach, a Gaussian-Fourier series, composed of a limited number of components, is used to approximate a ground motion, and the parameters of Gaussian components are determined through solving a nonlinear global optimization problem. Eventually, two ensembles of ground motions, including 40 near-fault and 44 far-fault ground motions, are used to demonstrate the efficiency of the proposed method in identifying dominant components and the reconstruction of elastic and inelastic response spectra within a specific period range.

2. Ground Motion Decomposition

2.1 The limitations of conventional time-frequency analysis approaches

Fourier series is an archetypical feature extraction tool. Its extension to the Fourier integral transform, the discrete Fourier transform (DFT) and the fast Fourier transform (FFT) is the bedrock of most signal processing technologies [28]. The main disadvantage, for the case of pulse identification, is that we exchange time for frequency, and thus loose the ability to time-localise components. This can be ameliorated to some degree by employing the short-time Fourier transform (STFT) which trades resolution in time (via windowing) for resolution in frequency. However, due to Heisenberg's uncertainty principle, it is not possible to both maintain high time-resolution (to determine when in time a component occurs) while also maintaining high frequency-resolution (to determine the frequency of that component).

The Wigner-Ville transform (WVT) ([29], [30]) is another attempt at obtaining high time-resolution and frequency-resolution by making use of additional constraints. While this approach is attractive, it does result in interference terms, false peak artefacts (errors), and these may overlap with signal terms. By modifying the additional constraints (using for example the pseudo Wigner-Ville Transform (PWVT)), it is possible to intuit to some degree, which time-frequency peaks are components of the

signal and which are artefacts of the constraints. However, generally, it may be difficult to always accurately time-locate a pulse for any general time-series.

The discrete wavelet transform (DWT) decomposes a time series into a far smaller set of frequency band limited components than the discrete Fourier transform. Each wavelet level, also known as the detail and approximation components, is defined for frequency sub-bands that are progressively halved. For the case of a time series with 1024 points, the number of wavelet levels is somewhere between 5 and 10 depending on the mother wavelet. This compares favourably with 512 sinuisodal components, when one uses the FFT. Thus, the wavelet decomposition results in far fewer non-stationary components. Each wavelet level is essentially a cross-correlation function between any signal and the mother wavelet function. The mother wavelet is time-shifted and time-scaled (stretched/dilated), and then cross-correlated with the time series. A large value of the wavelet level at a particular point in time would suggest a larger correlation between mother wavelet (at that scale used) with the time series. Thus, the time locations of features in the time series that are correlated with the mother wavelet can be identified. However, the weakness of the DWT for pulse extraction is that the frequency-resolution is limited to the progressively halved frequency sub-bands. Therefore, it is preferable to employ the continuous wavelet transform (CWT), even though this is far less computationally efficient than the DWT. The CWT, $W_\psi x$, of a time series, $x(t)$, is defined as

$$\left[W_\psi x\right](\tau,\omega)=\sqrt{\omega}\int_{-\infty}^{\infty}x(t)\,\overline{\psi\left((t-\tau)\omega\right)}\mathrm{d}t \tag{1}$$

where $\overline{\psi(t)}$ is the complex conjugate of the mother wavelet function $\psi(t)$, ω introduces time-scaling and τ introduces time-shifting. This integral function (1) is a cross-correlation function between time series $x(t)$ and time-scaled/shifted wavelet $\psi\left((t-\tau)\omega\right)$.

Consider the Gabor wavelet that is defined as follows:

$$\psi(t:\tau,\omega,\sigma)=\exp\left(-\tfrac{1}{2\sigma^2}\left((t-\tau)\omega\right)^2\right)\exp\left(-\mathbf{i}(t-\tau)\omega\right) \tag{2}$$

where parameter σ controls the width of the 'bell-shaped' Gaussian. The Gabor wavelet is a Gaussian function modulated by a complex sinusoidal term. This mother wavelet is complex, the real part is symmetric and the imaginary part is anti-symmetric. It is worth comparing this with the Ricker (Mexican hat) wavelet:

$$\psi(t:\tau,\omega,\sigma)=\frac{2}{\pi^{0.25}\sqrt{3\sigma}}\exp\left(-\tfrac{1}{2\sigma^2}\left((t-\tau)\omega\right)^2\right)\left(1-\tfrac{1}{\sigma^2}\left(\omega(t-\tau)\right)^2\right) \tag{3}$$

which replaces the complex sinusoidal term with a real and symmetrical quadratic polynomial. The Ricker wavelet may appear attractive as the resulting cross-correlation (equation (1)) is real. However, the symmetry of this wavelet means using it introduces bias towards detecting symmetrical pulses. The Gabor wavelet (composed of both symmetrical and anti-symetrical components) is more general. Nevertheless, to plot the CWT, $W_\psi x$ (using the Gabor wavelet) requires ploting this function at some phase angle. Therefore, we are again back with the same problem of biasing the results towards a particular mix of symmetrical and anti-symmetrical pulses.

Figure 1 displays the absolute imaginary component of CWT, $W_\psi x$ function, for the Gabor wavelet and the ground motion no 1 of the near-fault ensemble (section 3.1) (for the case of pulse width parameter $\sigma=1$). Consider the series of maxima at around $(\tau=8,\omega/2\pi=2)$. The series of closely spaced maxima in the cross-correlation functions $\left|\mathrm{Im}\left(W_\psi x\right)\right|$ is caused by fixing a particular phase angle for this section through $W_\psi x$.

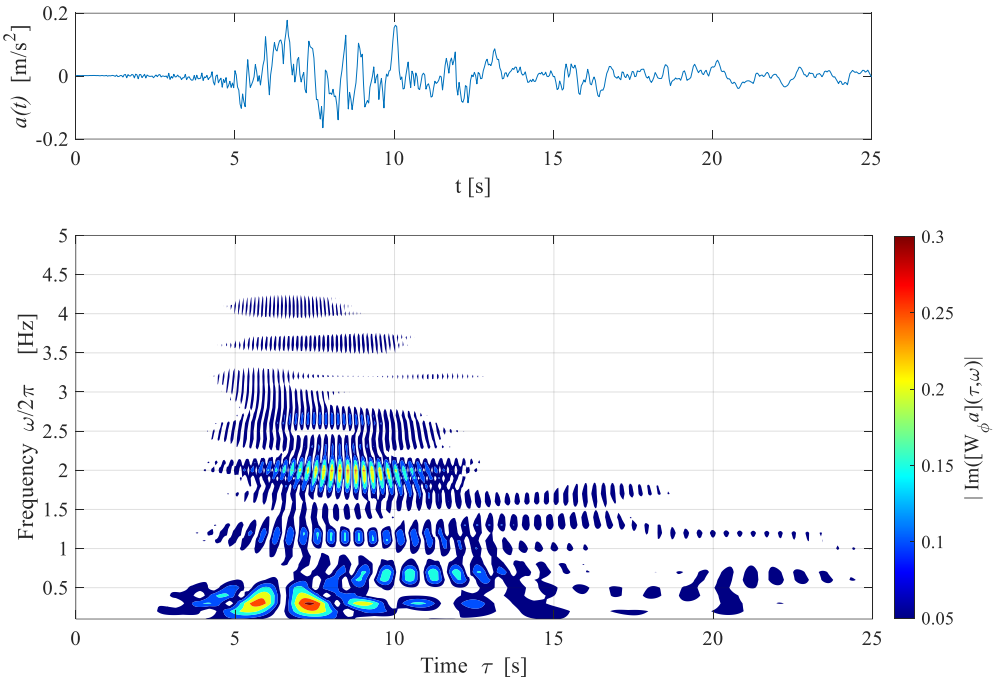

Figure 1. Absolute imaginary component of CWT for ground motion no 1 of the near-fault ensemble (section 3.1) and using a Gabor (Morlet) wavelet with $\sigma = 1$.

Thus, we have an ambiguity in precisely locating the position of a pulse. Therefore, the weaknesses of the CWT for pulse extraction are as follows:

(i) Only two parameters are modified, i.e. time-shifting τ and time-scaling $1/\omega$

(ii) The mother wavelet function choice is important e.g. if it is symmetric (like the Ricker wavelet), then it is biased towards the identification of symmetrical pulses and even for complex wavelets, like the Gabor wavelet, the problem of specifying a particular optimal phase angle remains.

(iii) The width of the wavelet scales with frequency ω, but it is adjusted by the arbitrary parameter σ (in both equations (2) and (3)). We need to specify σ and its optimal value is *a priori* unknown.

(iv) The use of the cross-correlation function, in the CWT, means we cannot determine a good match for the amplitude of the pulse. This is because the cross-correlation function normalisation removes the possibility of determining optimal amplitude scaling. Thus, we would need to adopt an additional least square fit process to determine the optimal amplitude for the pulse. Given these four problems, we chose to abandon conceptually the wavelet transform, and opt for a more brute-force global least squares fit approach, which gives the user complete freedom to identify position, frequency, phase and amplitude of the pulse within a time-series.

2.2 Global nonlinear least-squares using genetic algorithm

Let $a_0(t)$ represent a ground motion time history. This original ground motion is approximated by $\hat{a}_n(t)$, which is a partial, *n*-component, Gaussian-Fourier series of the following form:

$$\hat{a}_n(t) = \sum_{i=1}^{n} \hat{a}_i(t) \approx a_0(t) \tag{4}$$

$$\hat{a}_i(t : \tau_i, \omega_i, A_i, \sigma_i, \theta_i) = A_i \exp\left(-\frac{1}{2}\left(\frac{\omega_i (t - \tau_i)}{2\pi\sigma_i} \right)^2 \right) \sin(\omega_i t + \theta_i) \tag{5}$$

where $\tau_i, 1/\omega_i, A_i, \sigma_i$ and θ_i are time-shift, time-scale, amplitude-scale, pulse width, and phase angle respectively. This Gaussian-Fourier series can be viewed as an analogous (real) version of the

Gabor wavelet. Each Gaussian wave packet is defined in terms of five parameters. Hence, the equation (4) is defined by 5*n* parameters. The determination of these 5*n* parameters is a difficult numerical process. This nonlinear global optimization problem can be very arduous for even state-of-the-art solvers. The optimization toolbox in MATLAB [31] contains a number of different approaches using: (*i*) GlobalSearch, (*ii*) MultiStart, (*iii*) Patternsearch, (*iv*) Particleswarm, (*v*) Geneticalgorithm, and (*vi*) Simulated annealing. Regardless of which method is adopted, it would be impossible to fit an *n*-component Gaussian-Fourier series in a reasonable computational time on today's hardware. Thus, this problem is solved by seeking to fit just a single Gaussian-Fourier component at a time. Hence, one component $\hat{a}_i(t)$ at a time is determined by solving the following constraint optimization problem:

$$\begin{aligned} &\text{minimize} && F(\tau_i, \omega, A_{ii}, \sigma_i, \theta_i) = \left\| a_{i-1} - \hat{a}_i \right\|_2 \\ &\text{subject to:} && A_i \in \left[-\max(a), \max(a) \right] \\ & && \omega_i \in \left[2\pi/T_{\max}, 2\pi/T_{\min} \right] \\ & && \tau_i \in \left[0, t_d \right] \\ & && \sigma_i \in \left[0,1 \right] \\ & && \theta_i \in \left[0, 4\pi \right] \end{aligned} \tag{6}$$

where t_d is the duration of the ground motion; $T_{\min}$ and $T_{\max}$ are minimum and maximum periods of the Gaussian wave packet in the search process. These two periods specify a period range, which accounts for periods of dominant modes of the structure as well as the expected nonlinear, period elongation effects. In this work, the genetic algorithm approach is adopted as it is robust, relatively quick, reasonably accurate, and can handle problems with constraints. It was found that the GlobalSearch methods using fmincon() can produce fractionally better fits at an unreasonable computational expense. The equation (6) is solved using ga() MATLAB algorithm. The problem with using the ga() algorithm is that it is susceptible to the initial random seed. Therefore, to mitigate this effect, the ga() algorithm is run repeatedly ten times, and then, the best solution obtained is selected. While this appears computationally inefficient, in practice, it stabilizes the results, producing repeatability. Nevertheless, it is still far computationally more efficient than other global optimizers.

Once the first optimal wave packet is determined through the equation (6), it is subtracted from the original signal $a_{i-1}(t)$, defined in the equation (7):

$$a_i(t) = a_{i-1}(t) - \hat{a}_i(t) \tag{7}$$

Thus, the stages of this optimization are (i) determine a single optimal wave packet $\hat{a}_i(t)$ for a given target signal $a_{i-1}(t)$ (ii) subtract this optimal wave pack $\hat{a}_i(t)$ from the target signal $a_{i-1}(t)$ to obtain a new target signal $a_i(t)$ and (iii) repeat until the *n*-component Gaussian-Fourier wave packets are determined.

Note that this piecemeal solution to the problem is sequence-dependent. All MATLAB global optimization algorithms will attempt to find the apparent global optima in a given finite time or function evaluations. This process does not guarantee a global optimum. The internal path of the search is not defined by the user. The algorithms, and notably the genetic algorithm, does not always follow the same path when an analysis is repeated. Thus, the sequence of extracted wave packets is not necessarily unique or magnitude sorted. Therefore, after all the required Gaussian wave packets are extracted, they are rank sorted according to their Euclidean norm.

3. Application of Proposed Method

In this section, 84 ground motions are used (section 3.1) to demonstrate the application of the proposed method in decomposition and minimal representation of ground motions (section 3.2), as well as reconstruction of elastic and inelastic response spectra (section 3.3).

3.1 Ground motion database

In this work, two ensembles of ground motions are used. The first ensemble comprises 40 near-fault ground motions, and the second ensemble is composed of 44 far-fault ground motions. The 40 near-fault ensemble [15] is given in Appendix, Table 1. The 44 far-fault ensemble is given in FEMA P659 [32] and contains 22 pairs of horizontal ground motions from sites located within a distance greater than 10 km from fault rupture (see Appendix, Table 2).

3.2 Decomposition results and discussion

The application of the decomposition method proposed in section 2 is demonstrated here. The minimum and maximum periods for the component extraction are taken as 0.1 s and 1.5 s, respectively. This is because the periods of the extracted components fall within the period range of ordinary structures ([33], [8]). Figure 2 shows the ability of the proposed method to reconstruct original ground motion no.1 of the near-fault ensemble, where 1 to 5 decomposed components are used (e.g. components of the Gaussian-Fourier wave packet function in equations (4) and (5)). Figures 2(a)-2(e) illustrate the reconstructed acceleration time history. The higher number of components results in a better reconstruction of the ground motion. This is seen clearly in the elastic acceleration response spectra of the original and reconstructed ground motion shown in Figures 2(f)-2(j). A larger number of components gives a better reconstruction of the elastic response spectrum too. The first component reconstructs the peak spectral acceleration around the period of 0.5 s (Figure 2(f)), and the second component improves the response spectrum approximation for longer periods (Figure 2(g)). The third component captures the second peak (Figure 2(h)), and the fourth component reconstructs spectral accelerations at lower periods (Figure 2(i)). The signal in Figure 2(e) does not look visually similar to the waveform conventionally expected for a recorded earthquake. Nevertheless, the elastic response spectrum fits reasonably well using just the first five largest Gaussian wave packet components, as seen in Figure 2(j).

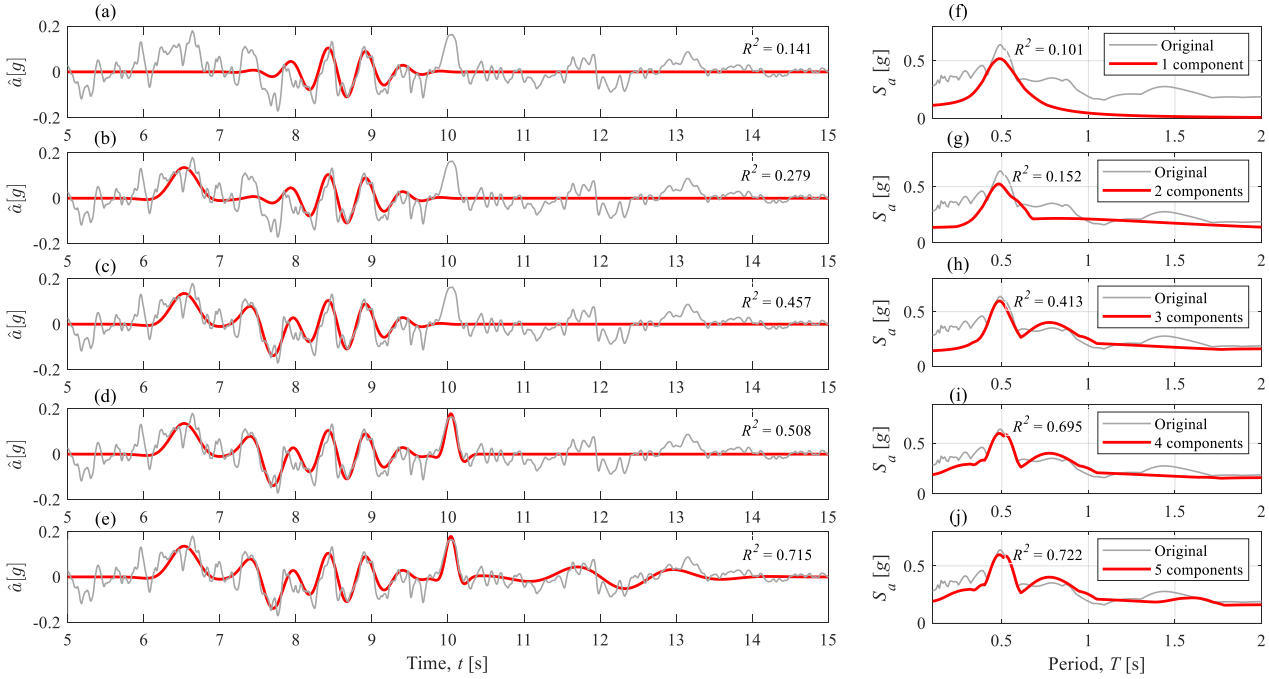

Figure 2. Reconstruction of ground motion no. 1 of the near-fault ensemble and its corresponding elastic response spectrum: (a) 1 component ground motion, (b) 2 components ground motion, (c) 3 components ground motion, (d) 4 components ground motion, (e) 5 components ground motion, (f) 1 components response spectrum, (g) 2 components response spectrum, (h) 3 components response spectrum, (i) 4 components response spectrum, and (j) 5 components response spectrum.

Figure 3 compares the acceleration time history and elastic acceleration response spectrum of the ground motion no.1 of the near-fault ensemble with those of the reconstructed ground motion using 15 components. It shows that the proposed method can capture very well the underlying frequency

banded trends in the peak ground motion values while maintaining time localization (see Figure 3(a)). Additionally, it estimates the elastic response spectrum of the original ground motion with a good tolerance over a wide range of periods. Note that the high-frequency content (above 5Hz) constitutes most of the difference in the fit (in the time-domain). Other than for the case of very stiff structures, this high-frequency content acts as noise on a much lower frequency underlying trend signal.

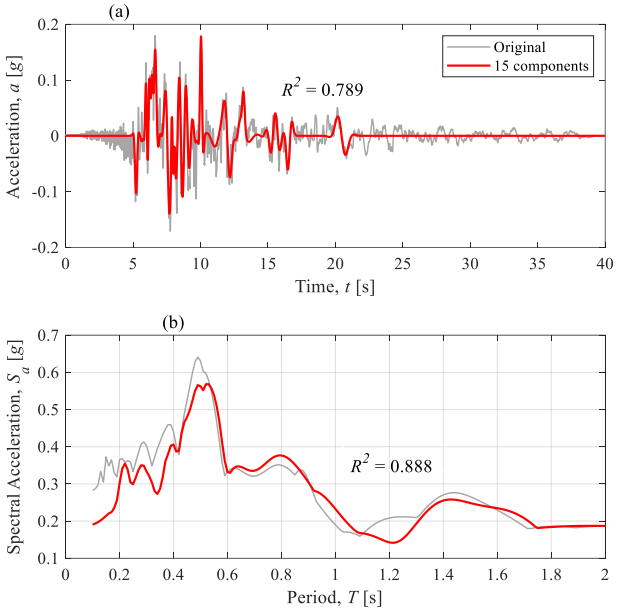

Figure 3. Reconstruction of: (a) ground motion no. 1 of the near-fault ensemble, and (2) its corresponding linear elastic response spectrum, using 15 components.

Figure 4 compares the velocity and displacement time histories and their corresponding response spectra of the ground motion no.1 of the near-fault ensemble with those of the reconstructed ground motion using 15 components. Unlike the acceleration time history, the velocity time history contains less high-frequency components, and hence, the low-frequency decomposed components approximate the original velocity time history with a higher accuracy (Figures 4(a) and 4(c)). Further, the displacement time history is mostly composed of low-frequency components, and thus, a more accurate reconstruction is achieved (Figures 4(b) and 4(d)).

Figures 5(a)-5(e) show the parameters of the extracted components for the exemplar ground motion in Figure 3. The amplitude of the components, A_i, could be positive or negative depending on capturing the best fit to the ground motion (Figure 5(a)). The circular frequency of the extracted components, ω_i, falls within the range of 4.2 rad/s to 26.1 rad/s (Figure 5(b)), which corresponds to the period range of 0.24s to 1.5 s, respectively. The phase of each component (Figure 5(c)), θ_i. the time-shift parameter, τ_i (Figure 5(d)) localizes each component in the time domain (the feature that is averaged out and 'lost' in the Fourier Transform), and the variance, σ_i, characterizes the width of the components (Figure 5(e)). As shown in Figure 5(f), the fit quality of each component (i.e. the ratio of Euclidean norm of the component-to-original ground motion), reduces as the number of the component increases. This was expected as the components are ranked sorted based on their Euclidean norm.

Unlike other intensity measures such as peak acceleration, peak velocity, and ordinates of spectral acceleration, input energy simultaneously reflects multiple characteristics and strength of a ground motion ([22], [23], [24]). So, the *i*th component-to-original ground motion energy ratio, β_i, for the near-fault and far-fault ensembles, is given by:

$$\beta_i = \frac{\int \left(\hat{a}_i(t)\right)^2 \mathrm{d}t}{\int \left(a_0(t)\right)^2 \mathrm{d}t} \tag{8}$$

Moreover, the cumulative energy ratio is determined by:

$$\beta_i^c = \frac{\int \sum_{j=1}^{i} \left(\hat{a}_j(t)\right)^2 \mathrm{d}t}{\int \left(a_0(t)\right)^2 \mathrm{d}t} \tag{9}$$

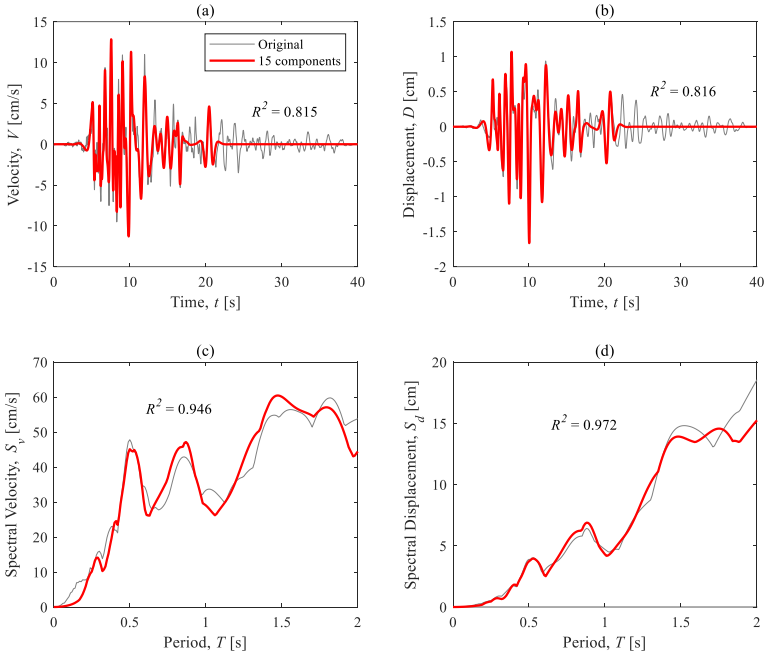

Figure 4. Reconstruction of ground motion no. 1 of the near-fault ensemble: (a) velocity time history, (2) displacement time history, (3) elastic velocity spectrum, and (4) elastic displacement spectrum, using 15 components.

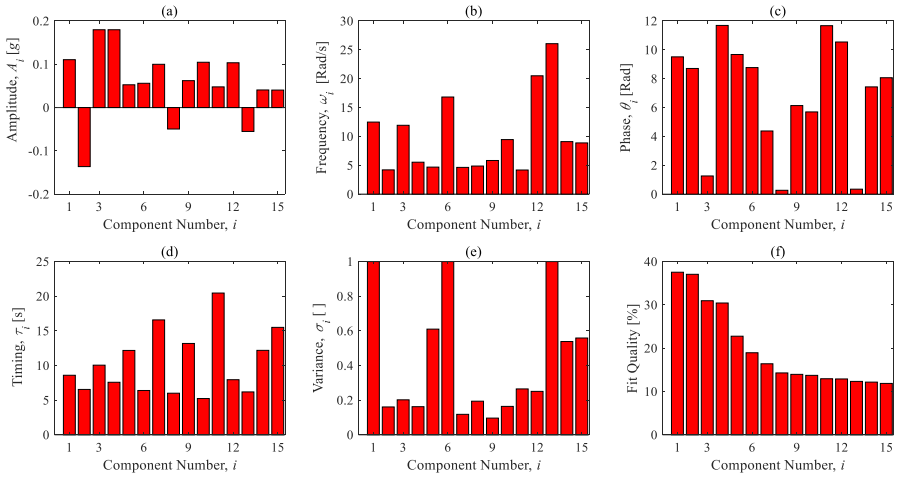

Figure 5. Parameters of each component for ground motion no. 1 of the near-fault ensemble: (a) amplitude, (b) circular frequency, (c) phase, (d) timing, (e) variance, and (f) fit quality.

The energy ratio and cumulative energy ratio of each component depends on the frequency (or period), variance, and amplitude of the component. Figure 6 shows the energy ratio and cumulative energy ratio for the first 30 extracted components of the near-fault and far-fault ensembles. As seen in Figures 6(a) and 6(b), for both ground motion ensembles, the energy ratio reduces for higher components. For component numbers larger than 10, the energy ratio is less than 5% for both ground motion ensembles, and hence, only the first 10 components of a ground motion could suffice to reconstruct the original ground motion with reasonable accuracy within the period range of 0.1-1.5 s.

It should be noted that the ground motion might contain high-energy ratio components outside the period range of interest. As seen in Figures 6(c) and 6(d), the cumulative energy ratio reaches over 90% for some ground motions using only the first few components, which means high-energy components of these ground motions exist within the range of 0.1-1.5 s. These ground motions are visually located at the top of Figures 6(c) and 6(d). For example, for the topmost cumulative energy ratio, ground motion no. 17 (see Figure 6(c)), 90% of the total energy of the ground motion is reached using the first eight components within a period range of 0.1-1.5 s. However, for some ground motions, even using the first 30 components, the cumulative energy ratio does not exceed 60%, which implies some high-energy components of these ground motions fall outside the used period range. These ground motions are visually located at the bottom of Figures 6(c) and 6(d). For example, for the bottom-most cumulative energy ratio, ground motion no. 12 (Figure 6(c)), the cumulative energy ratio reaches 46% using the first 30 components.

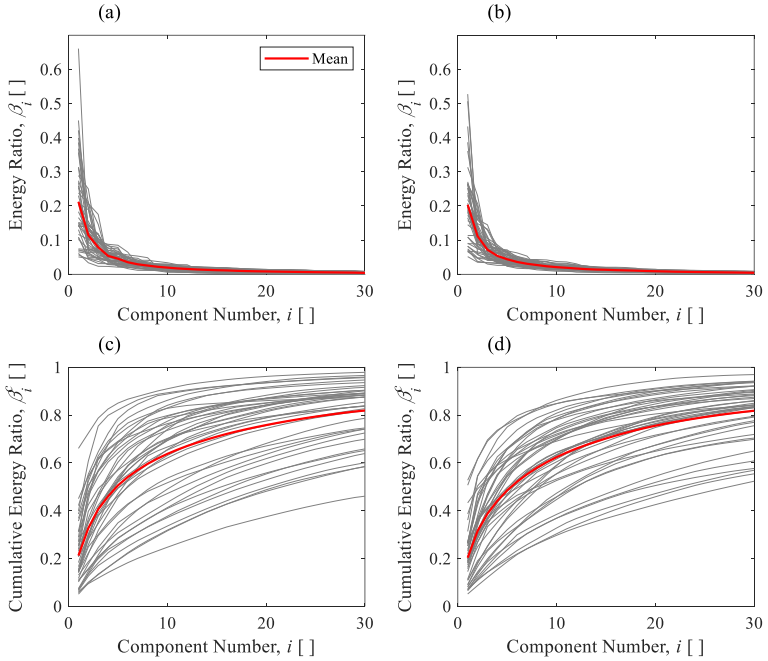

Figure 6. (a) The component-to-original energy ratios, near-fault ensemble, (b) component-to-original energy ratios, far-fault ensemble, (c) cumulative component-to-original energy ratios, near-fault ensemble, and (d) cumulative component-to-original energy ratios, far-fault ensemble. [ ] implies a unit-less quantity on axis.

An alternative widely used intensity measure is the Cumulative Absolute Velocity (CAV), which shows the continuous accumulation of the acceleration during an earthquake ([34], [35]). The *i*th component-to-original ground motion CAV ratio, Γ_i, for the near-fault and far-fault ensembles, is given by:

$$\Gamma_i = \frac{\int \left|\hat{a}_i(t)\right| \mathrm{d}t}{\int \left|a_0(t)\right| \mathrm{d}t} \tag{10}$$

and, the cumulative energy ratio is determined by:

$$\Gamma_i^c = \frac{\int \left|\sum_{j=1}^{i} \hat{a}_j(t)\right| \mathrm{d}t}{\int \left|a_0(t)\right| \mathrm{d}t} \tag{11}$$

Figure 7 shows the CAV ratio and cumulative CAV ratio for the first 30 extracted components of the near-fault and far-fault ensembles. As seen in Figures 7(a) and 7(b), like with energy ratios, the CAV ratios generally reduces for higher components. However, the energy ratio and cumulative

energy ratio curves are smoother compared to the CAV ones. This is because the CAV ratio curves contain more high-frequency components caused by the slope-discontinuity introduced by the absolute function.

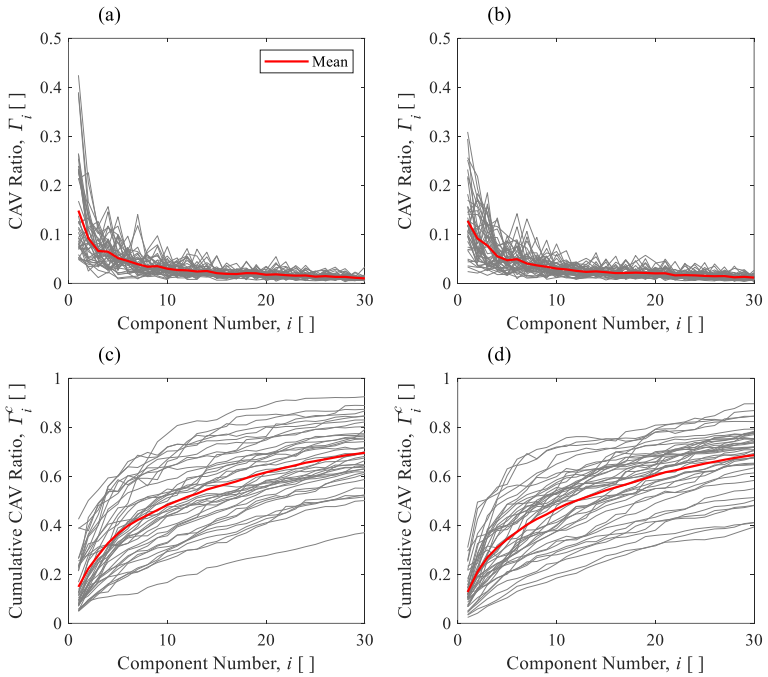

Figure 7. (a) The component-to-original CAV ratios, near-fault ensemble, (b) component-to-original CAV ratios, far-fault ensemble, (c) cumulative component-to-original CAV ratios, near-fault ensemble, and (d) cumulative component-to-original CAV ratios, far-fault ensemble.

The capability of the proposed method to detect dominant components of a ground motion within a specific period range is very beneficial in the seismic analysis of structures. A single dominant component is not necessarily a good representative of the original ground motion for the purpose of structural analysis. For linear structural systems more modes play a significant role in the total structural response. For nonlinear structural system fewer 'modes' play a significant role but these 'modes' change their frequencies with increasing ductility. Hence for both linear and nonlinear systems, it is unlikely that a single pulse (frequency component) will be sufficient in general.

Figures 8 and 9 show periods, amplitudes, and energy ratios of the near-fault and far-fault ensembles for the first three components. The extracted periods are within the range of 0.1-1.5 s, as mentioned above. The decomposition can be carried out for a narrow/wider range of periods if required. The period range of the decomposition depends on the fundamental period of the structure, intended for nonlinear seismic analysis. Comparing the periods and amplitudes of the extracted components demonstrates that higher components do not necessarily give shorter periods (higher frequencies) or larger amplitudes (see Figures 8(a)-8(f) and 9(a)-9(f)). However, from the energy ratio of the components, it is clear that higher components have lower energy ratios (see Figures 8(g)-8(i) and 9(g)-9(i)). This means that the dominant components of a ground motion are those, which collectively generate most of the total energy of the original ground motion. Therefore, using the proposed decomposition method here, the energy ratio of the components can be interpreted as the pulse indicator of the component. A larger energy ratio of the component shows a higher pulse feature of the component. This interpretation is regardless of whether the ground motion is a near-fault or far-fault record. In particular, for ground motion no 17, 18, and 6 of the near-fault ensemble, the first component provides 66%, 45%, and 42% of the total energy of the ground motion, respectively (see Figure 8(g)). On the other hand, for ground motion no. of 36, 6, and 39 of the far-fault ensemble, the first component contains 53%, 50%, and 43% of the total energy of the ground motion, respectively (see Figure 9(g)).

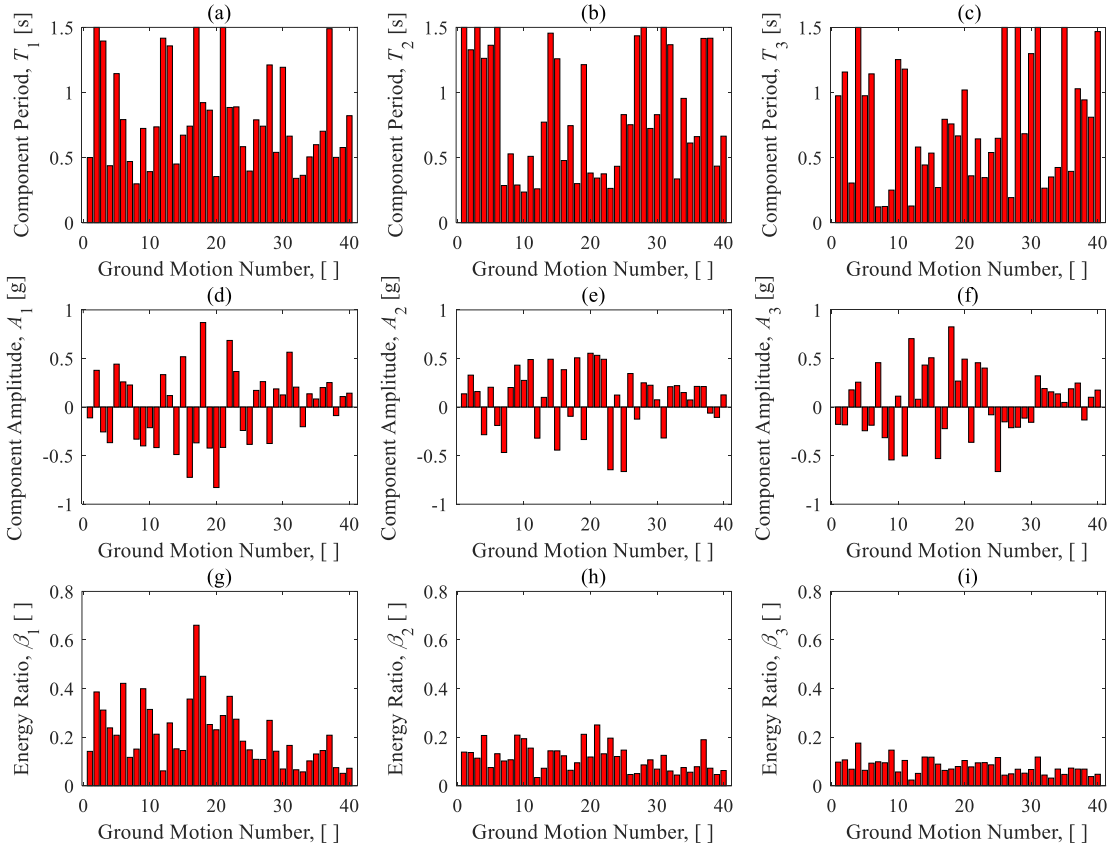

Figure 8. The properties of the first three components for the near-fault ensemble: (a) periods of the first component, (b) periods of the second component, (c) periods of the third component, (d) amplitudes of te first component, (e) amplitudes of the second component, (f) amplitudes of the third component, (g) energy ratios of the first component, (h) energy ratios of the second component, and (i) energy ratios of the third component.

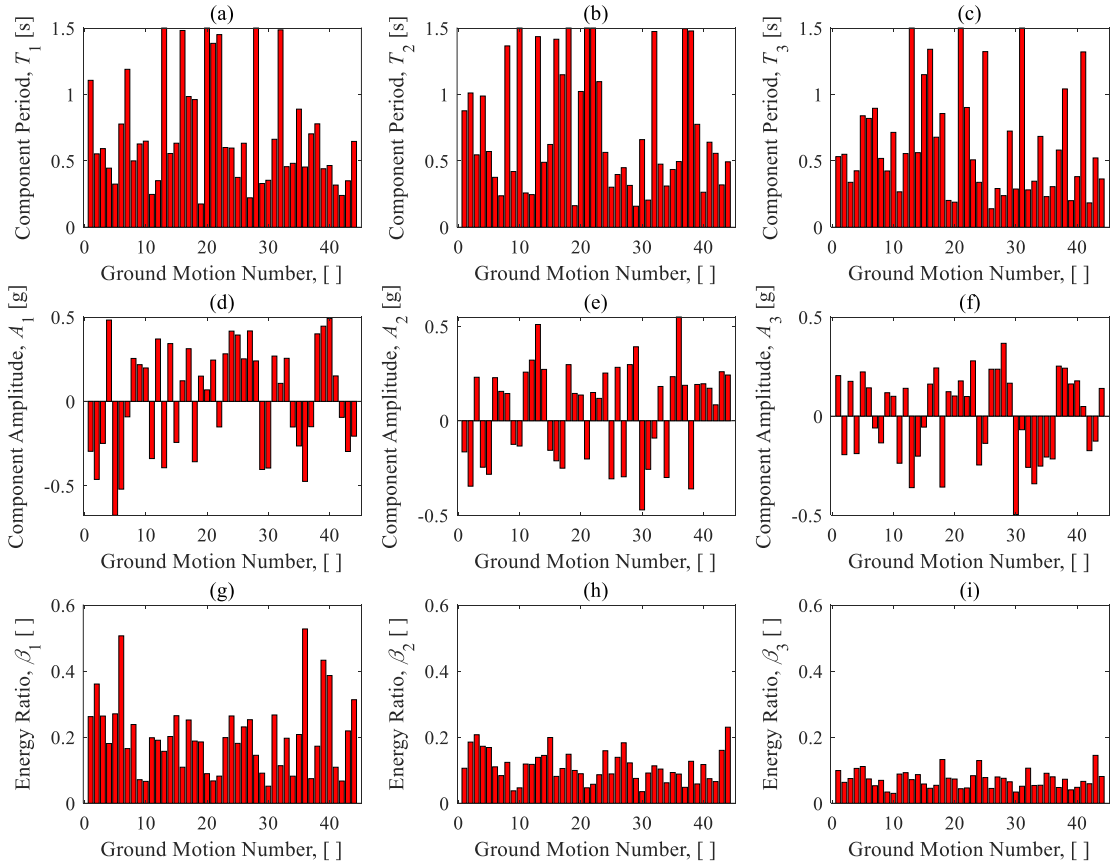

Figure 9. The properties of the first three components for the far-fault ensemble: (a) periods of the first component, (b) periods of the second component, (c) periods of the third component, (d) amplitudes of the first component, (e) amplitudes of the second component, (f) amplitudes of the third component, (g) energy ratios of the first component, (h) energy ratios of the second component, and (i) energy ratios of the third component.

3.3 Comparison of elastic response spectra

The proposed method in section 2 is adopted to reconstruct elastic and inelastic response spectra of the near-fault and far-fault ensembles. Figure 10 shows the elastic acceleration response spectra of the original and reconstructed ground motions for the near-fault and far-fault ensembles. The original elastic acceleration response spectra are shown in Figures 10(a) and 10(c), for near-fault and far-fault ensembles, respectively. The corresponding reconstructed elastic acceleration response spectra are illustrated in Figures 10(b) and 10(d) using the first 15 components. Comparing the original and reconstructed elastic acceleration response spectra for both near-fault and far-fault ensembles shows the robustness of the proposed method in replication of elastic acceleration response spectrum for a ground motion. This is seen more clearly when we compare the mean original and mean reconstructed acceleration response spectra for both near-fault and far-fault ensembles (see Figures 10(e) and 10(f)). Figure 11 compares mean elastic acceleration response spectra of the original and reconstructed ground motions with a different number of components for near-fault and far-fault ensembles. As seen, a higher number of components captures more features of the original ground motions, and thus, a more precise elastic response spectrum is reconstructed.

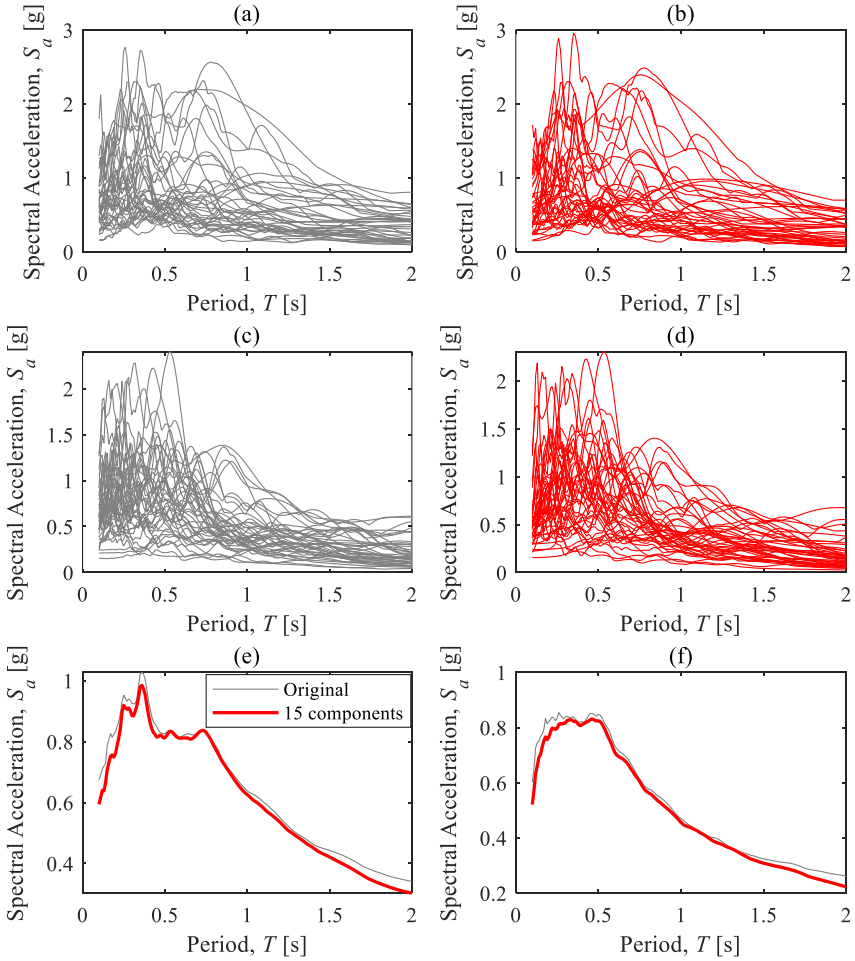

Figure 10. Elastic acceleration response spectra for: (a) original near-fault ensemble, (b) 15-component near-fault ensemble, (c) 15-component far-fault ensemble, (d) 15-component far-fault ensemble, (e) mean near-fault ensemble, and (f) mean far-fault ensemble.

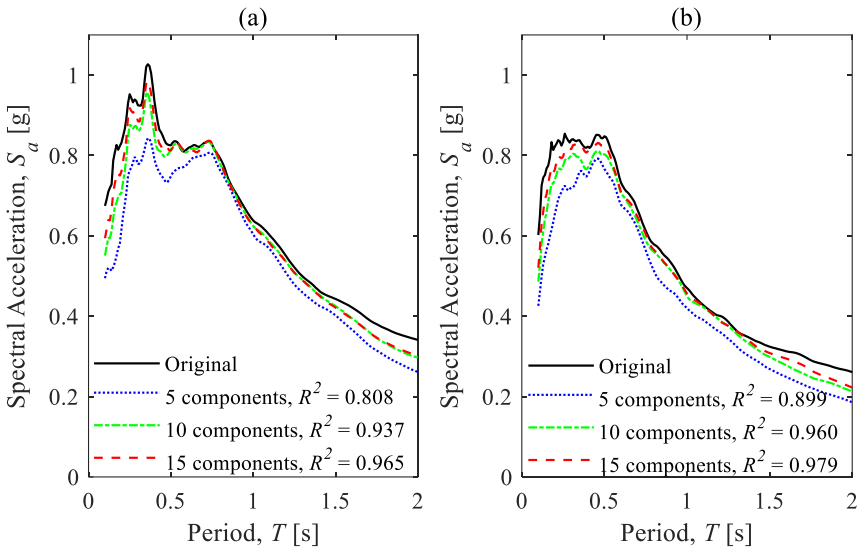

Figure 11. Mean elastic acceleration response spectra for original, 5, 10, and 15 components: (a) near-fault ensemble, and (b) far-fault ensemble.

3.4 Comparison of inelastic response spectra

For the construction of inelastic response spectra in this study, the single degree of freedom (SDOF) with the Bouc-Wen hysteresis model is analyzed. Both near-fault and far-fault ensembles are used as input. The non-dimensionalized hysteretic Bouc-Wen model ([36],[37],[38]) is used to model the inelastic behaviour of SDOF structures:

$$\ddot{\mu} + 2\xi\omega\dot{\mu} + \omega^2 f\left(\mu,\dot{\mu}\right) = -\frac{a_g}{u_y} \tag{9}$$

where ξ is damping ratio; ω is the circular frequency of the structure; μ is ductility, u/u_y, in which u is displacement, and u_y is the displacement at which the system exhibits yield; $f\left(\mu,\dot{\mu}\right)$ is the normalized nonlinear (hysteretic) force and a_g is the ground motion accelerogram. To specify yield, we define the total acceleration response at the yield $a_{Ty} = \omega^2 u_y$, and hence $u_y = a_{Ty}/\omega^2$. a_{Ty} is taken $0.3g$ in this study. Conventionally, in the standard Bouc-Wen model form, the normalized nonlinear force is given by:

$$f\left(\mu,\dot{\mu}\right) = \alpha\mu + \left(1-\alpha\right)z \tag{10}$$

where the internal degree of freedom z is defined by:

$$\dot{z} = \frac{1}{1+\delta_r\varepsilon}\left(B - \left(1+\delta_v\varepsilon\right)\left(\gamma\,\mathrm{sgn}\left(\dot{\mu}z\right) + \lambda\right)\left|z\right|^r\right)\dot{\mu} \tag{11}$$

where B,γ,λ,r are dimensionless parameters that control the shape of the hysteretic loops; δ_v and δ_r are dimensionless parameters that incorporate strength and stiffness degradation, respectively; ε is the normalized dissipated energy:

$$\varepsilon = \left(1-\alpha\right)\int_0^t z\dot{\mu}\mathrm{d}t \tag{12}$$

Often $B = 1 = \lambda + \gamma$ is considered for smooth softening hysteretic characteristics of structures ([39],[40],[41]). For degradation parameters, these ranges have been recommended: $\delta_r \in \left[0, 0.3\right]$ and $\delta_v \in \left[0, 0.05\right]$ ([42],[43]). In this work, δ_r and δ_v are taken 0.05 and 0.15, respectively. Figure 12 shows inelastic analysis results of an SDOF with a period of 0.75 s subject to ground motion no. 1 of the near-fault ensemble with a scale factor of 0.5g. As particularly seen in Figure 12(c), the ductility

reaches a maximum value of around 4, and the behaviour of the Bouc-Wen hysteresis model is shown in Figure 12(a).

Figure 13 shows the inelastic acceleration response spectra of the original and reconstructed ground motions for the near-fault and far-fault ensembles. The original inelastic response spectra are shown in Figures 13(a) and 13(c), for the near-fault and far-fault ensembles, respectively. The corresponding reconstructed inelastic response spectra are illustrated in Figures 13(b) and 13(d) using the first 15 components. As seen, the reconstructed inelastic acceleration response spectra approximate well the original ones for both near-fault and far-fault ensembles. Further, the mean reconstructed inelastic acceleration response spectrum is compared with its original counterpart for the near-fault and far-fault ensembles in Figures 13(e) and 13(f). Also in this case a very good match is observed between the mean original and reconstructed inelastic acceleration response spectra.

Figure 14 shows the mean inelastic acceleration and ductility response spectra. The 5-component acceleration response spectrum is in good agreement with the original response spectrum for the far-fault ensemble (see Figure 14(b)), while for the near-fault ensemble, a higher number of components (around ten components) is required to reach a good match for the acceleration response spectra (see Figure 14(a)). Additionally, the reconstructed ductility response spectrum gives a good fit using the five components for the near-fault ensemble (see Figure 14(c)). However, for the far-fault ensemble, using even 15 components is not sufficient, and a higher number of components needs to be considered to reach a precise fit. For the ductility and acceleration demands, a different number of components is needed to reach a good match with the original response spectra.

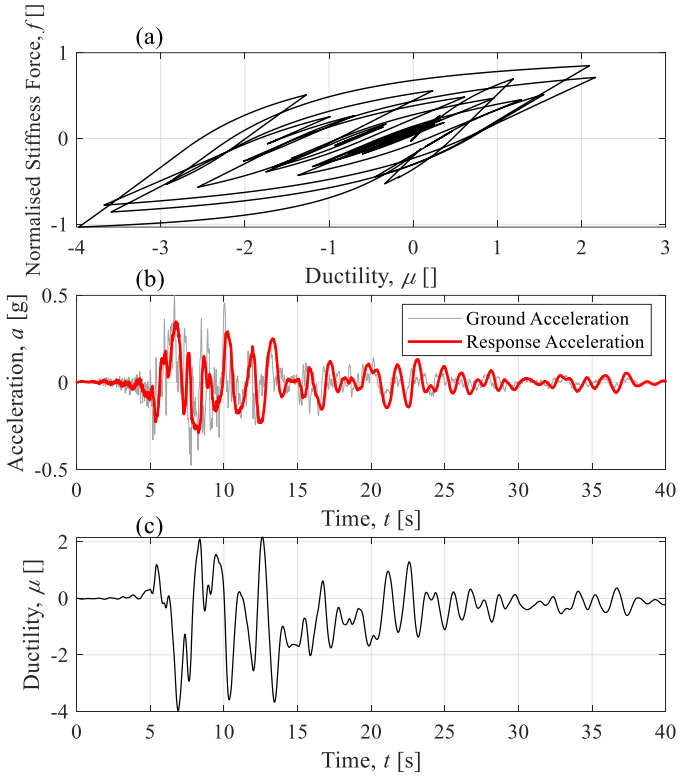

Figure 12. Bouc-Wen model results for an SDOF structure with a period of 0.75 s subject to ground motion no. 1 of the near-fault ensemble with the scale factor of 0.5g: (a) non-dimensionalized stiffness force versus ductility, (b) the ground motion and response acceleration, and (c) ductility time history.

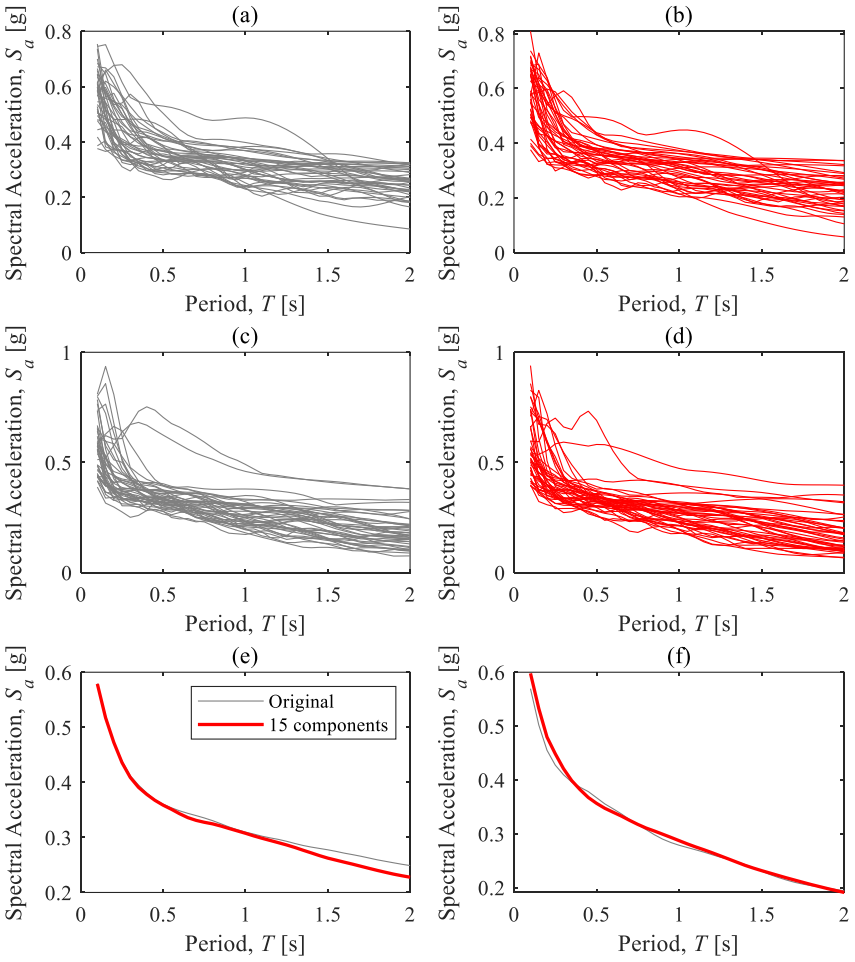

Figure 13. Inelastic acceleration response spectra for: (a) original near-fault ensemble, (b) 15-component near-fault ensemble, (c) original far-fault ensemble, (d) 15-component far-fault ensemble, (e) mean near-fault ensemble, and (f) mean far-fault ensemble.

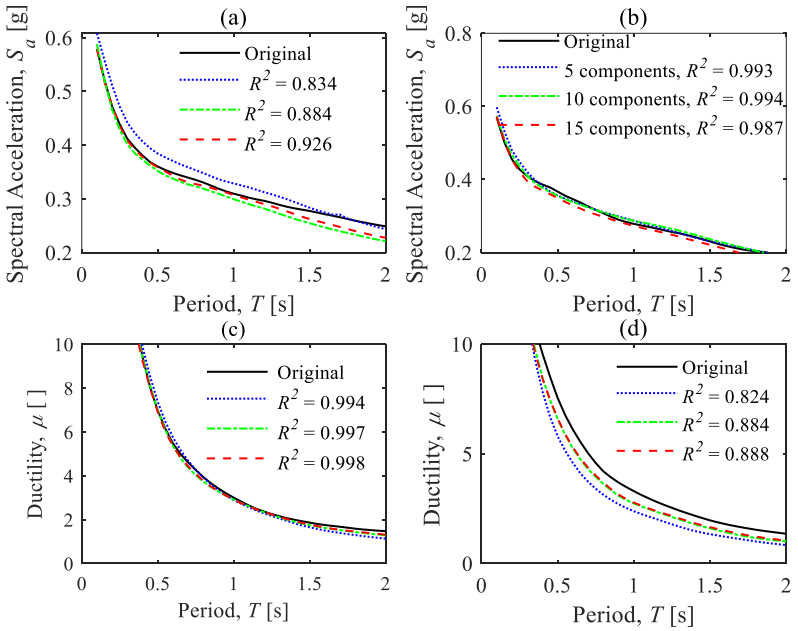

Figure 14. Mean inelastic for original, 5, 10, and 15 components: (a) acceleration, near-fault ensemble, (b) acceleration, far-fault ensemble, (c) ductility, near-fault ensemble, and (d) ductility, far-fault ensemble.

4. Conclusions

In this study, a new method is proposed to represent a ground motion with a minimal number of time-localized wave-packet components within a specific period range. A Gaussian-Fourier series is used to approximate the original ground motion. The parameters of this series are obtained by solving a nonlinear global optimization problem using a genetic algorithm approach. To demonstrate the accuracy and efficiency of the proposed method, two ensembles of ground motions, including one 40 near-fault and one 44 far-fault ground motions are used, and the reconstructed ground motions and response spectra are compared with their original counterparts.

The elastic and inelastic response spectra of the original ground motions and those from the proposed method were generated for the near-fault and far-fault ensembles. It was found that the elastic response spectra of the original ground motion can be regenerated within a reasonable precision, and the number of components of the approximation depends on the frequency content of the ground motion and the period range selected. The inelastic responses, obtained using a Bouc-Wen model, also showed that the partial Gauss-Fourier decomposition could accurately replicate the inelastic response spectra. Overall, the proposed method was seen to be very efficient and precise in the reconstruction of a ground motion and its corresponding response spectra with a minimal number of components.

Thus, we observe that, in general, earthquakes cannot be accurately characterized by a single pulse-like component. For linear systems, many more components are necessary, namely, on average, as many as ten pulse-like components may be required to match response accelerations across a whole spectrum. In contrast, for nonlinear structural responses, only five pulse-like components may be required on average to match ductility demand across a whole spectrum. A comparison between the mean ductility demand spectra for the near-fault and far-fault records suggests that the near-fault records, on average, can be successfully approximated by far fewer pulse components. This suggests that the near-fault records are more pulse-like with respect to ductility demand. This opens up an alternative metric for the selection of pulse-like records, namely, the records that five or fewer pulses can approximate.

For the case of a particular nonlinear structural system of known 'modal' frequencies, it is possible that fewer than 5, carefully selected, pulse-like components from a very narrow period range may be effective in the analysis. These critical pulses can be easily extracted using the proposed algorithm by specifying this narrow period range in the constraints of the global optimisation. This suggests that the ground motion acceleration time series contains a much simpler signal obscured by a lot of 'noise' which produces no significant structural responses. Many researchers have attempted to characterise ground motions as pulse-like or non-pulse-like by considering just a single pulse component of the ground motion. Results presented in this paper suggest, regrettably, that describing a ground motion as pulse-like or non-pulse-like must be done with reference to a specific period range (of the structural system it is forcing) and should not generally be done using just a single pulse component.

The current study applies the proposed method only to the elastic and inelastic SDOFs. Hence it is an open question what precisely the results will be for cases of real-life multi-degree-of-freedom structures with more complicated nonlinear behaviour. Thus, further research is required to investigate the performance of the method in approximation of a ground motion for real-life structures such as bridges, steel frames, and concrete shear walls.

References

[1] Takewaki I. Critical Excitation Methods in Earthquake Engineering: Second Edition. Elsevier 2013. https://doi.org/10.1016/C2012-0-06430-7.

[2] Kojima K, Takewaki I. Critical earthquake response of elastic–plastic structures under near-fault ground motions (Part 1: Fling-step input). Front Built Environ 2015; 1:1-11. https://doi.org/10.3389/fbuil.2015.00012.

[3] Kojima K, Takewaki I. Critical earthquake response of elastic–plastic structures under near-fault ground motions (Part 2: Forward-directivity input). Front Built Environ 2015: 1:1-13.

https://doi.org/10.3389/fbuil.2015.00013.
[4] Nazri FM, Alexander NA. Predicting collapse loads for buildings subjected to seismic shock. Bull Earthq Eng 2015; 13:2073-2093. https://doi.org/10.1007/s10518-014-9707-9.
[5] Beck JL, Papadimitriou C. Moving resonance in nonlinear response to fully nonstationary stochastic ground motion. Probabilistic Eng Mech 1993; 8:157-167. https://doi.org/10.1016/0266-8920(93)90011-J.
[6] Ge X, Alexander NA, Kashani MM. Rapid post-earthquake damage assessment of ageing reinforced concrete bridge piers using time-frequency analysis. Struct Infrastruct Eng 2020; 295: 1228-1244. https://doi.org/10.1080/15732479.2020.1801769.
[7] Kashani MM, Málaga-Chuquitaype C, Yang S, Alexander NA. Influence of non-stationary content of ground-motions on nonlinear dynamic response of RC bridge piers. Bull Earthq Eng 2017; 15: 3897–3918. https://doi.org/10.1007/s10518-017-0116-8.
[8] Li C, Kunnath S, Zuo Z, Peng W, Zhai C. Effects of early-arriving pulse-like ground motions on seismic demands in RC frame structures. Soil Dyn Earthq Eng 2020;130:105997. https://doi.org/10.1016/j.soildyn.2019.105997.
[9] Kohrangi M. Pulse - like versus non - pulse - like ground motion records : Spectral shape comparisons and record selection strategies 2019:46–64. https://doi.org/10.1002/eqe.3122.
[10] Alavi B, Krawinkler H. Behavior of moment-resisting frame structures subjected to near-fault ground motions. Earthq Eng Struct Dyn 2004; 33(6): 687-706. https://doi.org/10.1002/eqe.369.
[11] Alavi B, Krawinkler H. Consideration of Near-Fault Ground Motion Effects in Seismic Design. Proc. 12th World Conf. Earthq. Eng., 2000.
[12] Bray JD, Rodriguez-Marek A. Characterization of forward-directivity ground motions in the near-fault region. Soil Dyn Earthq Eng 2004; 24(11): 815-828. https://doi.org/10.1016/j.soildyn.2004.05.001.
[13] Dickinson BW, Gavin HP. Parametric Statistical Generalization of Uniform-Hazard Earthquake Ground Motions. J Struct Eng 2011; 137(3): 0733-9445. https://doi.org/10.1061/(asce)st.1943-541x.0000330.
[14] Vassiliou MF, Makris N. Estimating time scales and length scales in pulselike earthquake acceleration records with wavelet analysis. Bull Seismol Soc Am 2011;101:596–618. https://doi.org/10.1785/0120090387.
[15] Baker JW. Quantitative classification of near-fault ground motions using wavelet analysis. Bull Seismol Soc Am 2007; 97(5): 1486-1501. https://doi.org/10.1785/0120060255.
[16] Shahi SK, Baker JW. An empirically calibrated framework for including the effects of near-fault directivity in probabilistic seismic hazard analysis. Bull Seismol Soc Am 2011; 101(2): 742-755. https://doi.org/10.1785/0120100090.
[17] Chen X, Wang D, Zhang R. Identification of pulse periods in near-fault ground motions using the HHT method. Bull Seismol Soc Am 2019; 109(6): 2384–2398. https://doi.org/10.1785/0120190046.
[18] Liu Z, Li X, Zhang Z. Quantitative Identification of Near-Fault Ground Motions Based on Ensemble Empirical Mode Decomposition. KSCE J Civ Eng 2020. https://doi.org/10.1007/s12205-020-1491-2.
[19] Loh CH, Wu TC, Huang NE. Application of the empirical mode decomposition-Hilbert spectrum method to identify near-fault ground-motion characteristics and structural responses. Bull Seismol Soc Am 2001; 91 (5): 1339–1357. https://doi.org/10.1785/0120000715.
[20] Spanos PD, Giaralis A, Politis NP. Time-frequency representation of earthquake accelerograms and inelastic structural response records using the adaptive chirplet decomposition and empirical mode decomposition. Soil Dyn Earthq Eng 2007; 27(7): 675-689. https://doi.org/10.1016/j.soildyn.2006.11.007.
[21] Zhang Y, Hu Y, Zhao F, Liang J, Yang C. Identification of acceleration pulses in near-fault ground motion using the EMD method. Earthq Eng Eng Vib 2005; 4: 201–212.

https://doi.org/10.1007/s11803-005-0003-1.
[22] Wang T, Zhang M, Yu Q, Zhang H. Comparing the applications of EMD and EEMD on time-frequency analysis of seismic signal. J Appl Geophys 2012; 83:29-34. https://doi.org/10.1016/j.jappgeo.2012.05.002.
[23] Amiri GG, Rad AA, Hazaveh NK. Wavelet-Based Method for Generating Nonstationary Artificial Pulse-Like Near-Fault Ground Motions. Comput Civ Infrastruct Eng 2014; 29: 758–770. https://doi.org/10.1111/mice.12110.
[24] Kaveh A, Mahdavi VR. A new method for modification of ground motions using wavelet transform and enhanced colliding bodies optimization. Appl Soft Comput J 2016; 47: 357-369. https://doi.org/10.1016/j.asoc.2016.06.021.
[25] Khoshnoudian F, Ahmadi E, Sohrabi S. Response of nonlinear soil-MDOF structure systems subjected to distinct frequency-content components of near-fault ground motions. Earthq Eng Struct Dyn 2014; 43:701–716. https://doi.org/10.1002/eqe.2367.
[26] Khoshnoudian F, Ahmadi E. Effects of pulse period of near-field ground motions on the seismic demands of soil-MDOF structure systems using mathematical pulse models. Earthq Eng Struct Dyn 2013; 42:1565–1582. https://doi.org/10.1002/eqe.2287.
[27] Cooley JW, Tukey JW. An Algorithm for the Machine Calculation of Complex Fourier Series. Math Comput 1965; 297-301. https://doi.org/10.2307/2003354.
[28] Proakis JG, Monolakis DG. Digital signal processing: principles, algorithms, and applications. Pearson 1996.
[29] Cohen L. Time Frequency Analysis: Theory and Applications. Englewood Cliffs, NJ Prentice-Hall, 1995.
[30] Auger F, Flandrin P, Gonçalves P, Lemoine O. Time-Frequency Toolbox. 1996.
[31] Mathworks. Optimization Toolbox User's Guide R2017a. MATLAB Man 2017.
[32] FEMA P695. Quantification of Building Seismic Performance Factors. 2009.
[33] Sehhati R, Rodriguez-Marek A, ElGawady M, Cofer WF. Effects of near-fault ground motions and equivalent pulses on multi-story structures. Eng Struct 2011; 33(3): 767-779. https://doi.org/10.1016/j.engstruct.2010.11.032.
[34] Mashayekhi M, Estekanchi HE, Vafai A, Mirfarhadi SA. Simulation of Cumulative Absolute Velocity Consistent Endurance Time Excitations. J Earthq Eng 2021; 25(5) 892-917. https://doi.org/10.1080/13632469.2018.1540371.
[35] Wu MH, Wang JP, Chiang PE. Cumulative absolute velocity (CAV) seismic hazard assessment for Taiwan. J Earthq Eng 2020; 26(7): 3440-3460. https://doi.org/10.1080/13632469.2020.1803161.
[36] Meibodi AA, Alexander NA. Exploring a generalized nonlinear multi-span bridge system subject to multi-support excitation using a Bouc-Wen hysteretic model. Soil Dyn Earthq Eng 2020; 135: 106160. https://doi.org/10.1016/j.soildyn.2020.106160.
[37] Li H guang, Meng G. Nonlinear dynamics of a SDOF oscillator with Bouc-Wen hysteresis. Chaos, Solitons and Fractals 2007; 34(2): 337-343. https://doi.org/10.1016/j.chaos.2006.03.081.
[38] Song J, Der Kiureghian A. Generalized Bouc–Wen Model for Highly Asymmetric Hysteresis. J Eng Mech 2006; 132(6): 610-618. https://doi.org/10.1061/(asce)0733-9399(2006)132:6(610).
[39] Sivaselvan M V., Reinhorn AM. Hysteretic Models for Deteriorating Inelastic Structures. J Eng Mech 2000; 127(11): 633-640. https://doi.org/10.1061/(asce)0733-9399(2000)126:6(633).
[40] Charalampakis AE, Koumousis VK. Parameter estimation of Bouc-Wen hysteretic systems using a Sawtooth Genetic Algorithm. Proc. 5th Int. Conf. Eng. Comput. Technol., 2006. https://doi.org/10.4203/ccp.84.195.
[41] Giaralis A, Spanos PD. Derivation of equivalent linear properties of Bouc-Wen hysteretic systems for seismic response spectrum analysis via statistical linearization. 10th HSTAM Int Congr Mech 2013.
[42] Goda K, Hong HP, Lee CS. Probabilistic characteristics of seismic ductility demand of SDOF

systems with bouc-wen hysteretic behavior; 13(5): 600-622. J Earthq Eng 2009. https://doi.org/10.1080/13632460802645098.

[43] Ma F, Zhang H, Bockstedte A, Foliente GC, Paevere P. Parameter analysis of the differential model of hysteresis. J Appl Mech Trans ASME 2004; 71(3): 342-349. https://doi.org/10.1115/1.1668082.

Appendix

Table 1. The near-fault ground motion ensemble.

No	Earthquake Name	Year	Station Name	Magnitude
1	Imperial Valley-06	1979	EC County Center FF	6.53
2	Imperial Valley-06	1979	EC Meloland Overpass FF	6.53
3	Imperial Valley-06	1979	El Centro Array #4	6.53
4	Imperial Valley-06	1979	El Centro Array #5	6.53
5	Imperial Valley-06	1979	El Centro Array #6	6.53
6	Imperial Valley-06	1979	El Centro Array #7	6.53
7	Imperial Valley-06	1979	El Centro Array #8	6.53
8	Imperial Valley-06	1979	El Centro Differential Array	6.53
9	Morgan Hill	1984	Coyote Lake Dam (SW Abut)	6.19
10	Loma Prieta	1989	Gilroy - Gavilan Coll.	6.93
11	Loma Prieta	1989	LGPC	6.93
12	Landers	1992	Lucerne	7.28
13	Landers	1992	Yermo Fire Station	7.28
14	Northridge-01	1994	Jensen Filter Plant	6.69
15	Northridge-01	1994	Jensen Filter Plant Generator	6.69
16	Northridge-01	1994	Newhall - Fire Sta	6.69
17	Northridge-01	1994	Newhall - W Pico Canyon Rd.	6.69
18	Northridge-01	1994	Rinaldi Receiving Sta	6.69
19	Northridge-01	1994	Sylmar - Converter Sta	6.69
20	Northridge-01	1994	Sylmar - Converter Sta East	6.69
21	Northridge-01	1994	Sylmar - Olive View Med FF	6.69
22	Kobe, Japan	1995	KJMA	6.90
23	Kobe, Japan	1995	Takarazuka	6.90
24	Kocaeli, Turkey	1999	Gebze	7.51
25	Chi-Chi, Taiwan	1999	CHY028	7.62
26	Chi-Chi, Taiwan	1999	CHY101	7.62
27	Chi-Chi, Taiwan	1999	TCU049	7.62
28	Chi-Chi, Taiwan	1999	TCU052	7.62
29	Chi-Chi, Taiwan	1999	TCU053	7.62
30	Chi-Chi, Taiwan	1999	TCU054	7.62
31	Chi-Chi, Taiwan	1999	TCU068	7.62
32	Chi-Chi, Taiwan	1999	TCU075	7.62
33	Chi-Chi, Taiwan	1999	TCU076	7.62
34	Chi-Chi, Taiwan	1999	TCU082	7.62
35	Chi-Chi, Taiwan	1999	TCU087	7.62
36	Chi-Chi, Taiwan	1999	TCU101	7.62
37	Chi-Chi, Taiwan	1999	TCU102	7.62
38	Chi-Chi, Taiwan	1999	TCU103	7.62
39	Chi-Chi, Taiwan	1999	TCU122	7.62
40	Chi-Chi, Taiwan	1999	WGK	7.62

Table 2. The far-fault ground motion ensemble.

No	Component 1	Component 2	PGA_{max} (g)	PGV_{max} (cm/s)
1,2	NORTHR/MUL009	NORTHR/MUL279	0.52	63
3,4	NORTHR/LOS00	NORTHR/LOS270	0.48	45
5,6	DUZCE/BOL000	DUZCE/BOL090	0.82	62
7,8	HECTOR/HEC000	HECTOR/HEC090	0.34	42
9,10	IMPVALL/H-DLT262	IMPVALL/H-DLT352	0.35	33
11,12	IMPVALL/H-E11140	IMPVALL/H-E11230	0.38	42
13,14	KOBE/NIS000	KOBE/NIS090	0.51	37
15,16	KOBE/SHI000	KOBE/SHI090	0.24	38
17,18	KOCAELI/DZC180	KOCAELI/DZC270	0.36	59
19,20	KOCAELI/ARC000	KOCAELI/ARC090	0.22	40
21,22	LANDERS/YER270	LANDERS/YER360	0.24	52
23,24	LANDERS/CLW-LN	LANDERS/CLW-TR	0.42	42
25,26	LOMAP/CAP000	LOMAP/CAP090	0.53	35
27,28	LOMAP/G03000	LOMAP/G03090	0.56	45
29,30	MANJIL/ABBAR--L	MANJIL/ABBAR--T	0.51	54
31,32	SUPERST/B-ICC00	SUPERST/B-ICC090	0.36	46
33,34	SUPERST/B-POE270	SUPERST/B-POE360	0.45	36
35,36	CAPEMEND/RIO270	CAPEMEND/RIO360	0.55	44
37,38	CHICHI/CHY101-E	CHICHI/CHY101-N	0.44	115
39,40	HICHI/TCU045-E	CHICHI/TCU045-N	0.51	39
41,42	SFERN/PEL090	SFERN/PEL180	0.21	19
43,44	FRIULI/A-TMZ000	FRIULI/A-TMZ270	0.35	31